International Journal of Applied Mathematics
Volume 38 No. 6s, 2025
ISSN: 1311-1728 (printed version); ISSN: 1314-8060 (on-line version)

NEUROXL-CRFNET: A HYBRID TRANSFORMER–GRAPH FRAMEWORK FOR AUTOMATED HEPATOCELLULAR CARCINOMA HISTOPATHOLOGY CLASSIFICATION

M.Indumathi[1*] and Dr. M.Vanitha[2]
[1*]Ph.D Research Scholar, Department of Computer Applications, Alagappa University, Karaikudi, India, Mail id: mindumathi2@gmail.com
[2]Assistant Professor, Department of Computer Applications, Alagappa University, Karaikudi, India
Mail id: vanitham@alagappauniversity.ac.in

Abstract

In this research work, a novel deep learning-based framework for automated hepatocellular carcinoma (HCC) detection from histopathological images is introduced. The pipeline begins with a comprehensive pre-processing stage to enhance image quality and normalize color variability across slides. Macenko color normalization ensures stain-independent intensity profiles, while Gaussian filtering removes artifacts and de-noises tissue sections. Morphological operations segment the tissue regions of interest, after which image patches of size 256 × 256 px are extracted using an overlapping sliding window to capture diverse local features. For feature extraction, a Transformer-based IntentNet backbone models global contextual dependencies within each patch, producing rich attention-aware representations. The features are first ranked by Mutual Information (MI) to identify the most informative descriptors and then refined through a Hybrid Grey Wolf Optimizer (HGWO) that fuses Grey Wolf and Harris Hawk strategies for optimal feature subset selection. Finally, disease classification is performed by the proposed NeuroXL-CRFNet, a hybrid network that integrates a Neuro-Symbolic Graph Convolutional Network (NS-GCN) for structural feature reasoning, XLNet for contextual sequence modeling, and a Conditional Random Field (CRF) decoder for structured prediction. Extensive integration of these modules enables precise HCC detection, offering a robust, end-to-end solution for histopathological image analysis.

Keywords – medical image processing; hepatocellular carcinoma; deep feature extraction; Transformer-based IntentNet backbone; HGWO-MI feature selector; NeuroXL-CRFNet

1. Introduction

Biomedical imaging classification has become an interesting area of research, following a growing reliance on the use of medical imaging to identify, diagnose and treat disease [1]. The number of imaging paradigms like X-ray, CT, MRI, ultrasound and the use of personalized imaging, can generate significant amounts of data [2], which enhances the need for systems of organize for deeper analysis and classification of images [3]. The traditional classifications and diagnoses, rely on expert opinion, with variability stemming from subjective judgment, fatigue, and ability in identifying subtle patterns and structures in the image [4]. Biomedical image

Received: August 9, 2025

International Journal of Applied Mathematics
Volume 38 No. 6s, 2025
ISSN: 1311-1728 (printed version); ISSN: 1314-8060 (on-line version)

classification is important because it can potentially facilitate early diagnosis and improvements in healthcare system capacity [5]. Image classification differentiates normal appearance and abnormal appearance and classifies normal and abnormal appearance into potential disease categories [6] to help clinicians make accurate assessments earlier rather than later. Additionally, the evolution of computational techniques has broadened the scope for studying high-dimensional imaging data and discovering clinically important characteristics to improve disease prediction [7]. Accordingly, biomedical image classification represents a thriving intersection of medical imaging, data analytics, and clinical intervention that could influence practices and healthcare research [8].

Hepatocellular carcinoma is an important area of focus for biomedical image classification [9], as it is the most common primary liver cancer and is both common and presumably serious [10]. It is also important to detect HCC early in its development, where treatment options are limited and prognosis is poor [11]. Diagnostic imaging, including ultrasound, CT, and MRI, is at the forefront of diagnosing and monitoring HCC, informing tumour morphology and vascular and tissue characteristics [12]. Important to the classification of imaging and diagnosis of HCC, is the accurate classification of an imaging or scan for HCC as opposed to either a benign liver lesion or other cancer [13]. Accurate classification plans for intervention that can be timely, informed, and directive, thereby improving patient outcomes [14].

Biomedical image classification is an important area of medical research that enables consistent analysis of complex imaging modalities, including but not limited to, X-ray, CT, MRI, and ultrasound for the diagnosis of disease. It allows for a consistent, objective, and efficient way to classify medical images, which can facilitate early disease detection and treatment planning, both alongside its many challenges as a profession. One clear illustration of a popular application of medical imaging classification is in the study of hepatocellular carcinoma (HCC), which is the most common primary cancer of the liver. The challenge with this subtype of cancer is that it is often asymptomatic until the late stage of disease. As such, being able to develop a robust imaging-based classification method that can reliably distinguish between HCC and benign conditions is a priority for timely diagnosis and improving patient survival.

Although there have been many improvements in the technologies for medical imaging, accurate diagnosis of complex diseases like hepatocellular carcinoma is still a challenge due to the high variability in image quality, as well as subtle differences between benign and malignant lesions, and due in part to the time burden, variability, and potential errors associated with expert clinicians rendering a diagnosis from images. Consequently, this may lead to delays in diagnosis and treatment. Automated biomedical image classification strategies have emerged to surmount these challenges, leading to the analysis and classification of medical images consistently, efficiently, and accurately in consideration of a myriad of imaging databases. Automated classifications and analyses will identify complex patterns and features that are beyond human-level perception, leading to better early detection of disease, diagnostic errors, and clinical decision-making.

Received: August 9, 2025

International Journal of Applied Mathematics
Volume 38 No. 6s, 2025
ISSN: 1311-1728 (printed version); ISSN: 1314-8060 (on-line version)

The key contribution of this research work is:

- To iintroduce a new Transformer-driven IntentNet backbone model to histopathological HCC images, capturing both global context and fine-grained cellular morphology through multi-head self-attention.
- To develop of a novel hybrid optimization scheme combining Grey Wolf and Harris Hawk strategies to achieve an optimal feature subset, improving discriminative power while reducing dimensionality.
- To design an innovative NeuroXL-CRFNet classifier with Neuro-Symbolic Graph Convolutional Network (NS-GCN) for structural reasoning; XLNet for bidirectional contextual encoding, and Conditional Random Field (CRF) decoder for structured sequence prediction—delivering superior accuracy and interpretability.
- By combining symbolic graph reasoning with deep contextual embeddings, the proposed model offers transparent decision pathways and robust generalization across varying staining conditions and tissue morphologies.

The remaining section of this article is organized as: Section 2 discusses about the SOTA on HCC diagnosis, which the detailed description of the proposed approach for HCC. The comparative analysis made between the proposed and the existing works are manifested in Section 4 and this article is concluded in section 5.

2. Related Work:

Hepatocellular carcinoma (HCC) is a common type of liver cancer and the presence of high-dimensional, noisy and redundant clinical data decreases the accuracy and efficiency of conventional machine learning models, resulting in an arduous task to predict early and reliably. Mostafa, G., *et al* [15] introduces feature reduction such as weighting features, hidden feature correlation, feature selection, and optimized selection and combines it with a plethora of algorithms, including Naive Bayes, SVM, Neural Networks, Decision Tree, and KNN to extract the most important features and improve predictive performance. Importantly, the experimental results front the application of feature reductions as markedly improved accuracy, decreased execution time, and improved predictive performance, consistently outperforming algorithms trained on the original high-dimensional dataset, with post-reduction accuracies.

Early recurrence (ER) of HCC post-operatively is a leading cause of death, and predicting ER is difficult because most data relevant to painting a precise predictive picture is not annotated for use. This presents significant challenges, largely due to limited annotated medical imaging data, especially in relation to deep learning models that require a form of transfer learning to generalize effectively. To address these issues, Song, J., *et al* [16] used a multi-task self-supervised pre-training framework using the unlabelled images from our dataset, which consists of two components: phase shuffle for learning intra-image features, and case discrimination for learning inter-image features of the entire case to improve the feature representation and a subset of the data which does not require labelled data. Results show that our method outperforms transfer learning, single-task self-supervised pre-training, and

Received: August 9, 2025

International Journal of Applied Mathematics
Volume 38 No. 6s, 2025
ISSN: 1311-1728 (printed version); ISSN: 1314-8060 (on-line version)

DINOv2 pre-training for ER prediction, and improves the classification performance of focal liver lesions as well.

Predicting the response of HCC to Yttrium-90 (Y90) radiation segmentectomy accurately is challenging because currently available clinical parameters and alpha-fetoprotein (AFP) levels have limited predictive value, and therefore are not ideal for treatment planning. Stocker, D., *et al* [17] combines pre-treatment magnetic resonance imaging (MRI)-based radiomics features with clinical parameters and APR; then use logistic regression and cross-validation to provide better prediction accuracy. The findings show that the combined model outperforms either clinical parameters or AFP alone, which indicates that MRI radiomics can improve the prediction of HCC response after Y90 segmentectomy.

HCC poses challenges with accurate diagnosis, risk stratification, progression modelling, and clinical decision support, while clinical standards do not fully encompass these barriers. To overcome these barriers Larrain, C., *et al* [18] presented Emerging Artificial Intelligence (AI) techniques such as radiomics, machine learning, and deep learning will provide greater accuracy and personalization for support in supporting diagnosis, intra-operative support, predictive modelling, and imaging. Early studies have indicated that AI has a greater predictive accuracy in HCC incidence, progression, and surgical outcomes than standard models and are starting to demonstrate that AI will be a valuable aspect of holistic management of HCC.

Only some unresectable HCC patients derive clinical benefit from lenvatinib plus immune checkpoint inhibitors (CLICI treatment), and currently, there are no consistent predictors of treatment response. Therefore, Liao, N.Q., *et al* [19] developed an interpretable deep learning (DL) model based on multiphase CT imaging (arterial, portal and delayed phase) visualized on heatmaps for interpretability. The DL model provided enhanced performance over DL models using only uniphase or biphase inputs (AUC 0.802), and the portal phase was the most predictive of response, along with the identification of 6 imaging features. The DL model provides a usable imaging-based tool for reflexively guiding treatment options for patients undergoing CLICI treatment.

In developing countries, HCC continues to be a major contributor to death rates largely because of late diagnosis and inferior performance of traditional methods for diagnosis, including imaging, histopathology, biomarkers, and biopsy, which have limited sensitivity for early-stage detection. As a solution, Asif, A., *et al* [20] suggested artificial intelligence (AI) methods, particularly machine learning and deep learning, use images, pathology, biomarkers, and electronic health records to increase diagnostic accuracy, turnaround time, and accurately know the diagnosis to improve HCC diagnosis. AI-assisted models are reported to exceed traditional methods by providing greater sensitivity, specificity, and integration of multi-source data for more reliable and earlier HCC diagnosis.

While radical surgery is still the first-line treatment for HCC, HCC has one of the highest early recurrence rates with corresponding lack of prognostic modelling to successfully assess risk for extension to recurrence after surgical resection. In this study, a multimodal machine learning (ML) model incorporating clinical, radiomics, and pathomics features was developed

Received: August 9, 2025

ISSN: 1311-1728 (printed version); ISSN: 1314-8060 (on-line version)

and validated by Xie, Q., *et al* [21] using a cohort of 107 patients with HCC, with models built and comparisons made across feature groups and algorithms. A multimodal support vector machine (SVM) model outperformed competing models, and a nomogram was generated as a reproducible tool intended to benefit clinicians in the prediction of the likelihood of early recurrence of HCC and guide clinicians towards personalized treatment.

While histopathological image analysis is instrumental in the diagnosis and grading of hepatocellular carcinoma (HCC), its manual grading is time-consuming, subjective, and constrained by the nature of large area images. Zhang, J., *et al* [22] proposed a Dual Channel Attention-Sharing Hybrid Network (DCAH-Net), which incorporated convolutional neural networks (CNNs) to extract local features, transformers to model global features as well as an attention-sharing mechanism, in a patch based framework. The model outperformed existing models in the literature with a validation accuracy of 88.36%, taking into account precision and recall, and demonstrated generalizability for both retrospective and prospective studies across multiple medical datasets.

HCC is an ailment whose prognosis is improved with timely diagnosis and requires pathology of the liver. However, manual histopathology is a time-consuming and laborious method, and deep learning models normally rely on a large annotated dataset, which can be expensive. Lin, Y.S., *et al* [23] suggested to build a binary classifier for HCC image classification that utilizes GoogLeNet (Inception-V1) architecture for automation, coupled with an inverse power law model to establish an estimate of the minimum annotated image dataset size, for a range of reliable accuracy. The classifier was capable of achieving 91.37% accuracy, 92.16% sensitivity, and 90.57% specificity. Furthermore, the estimate provided a mechanism for determining the influence of dataset size on overall accuracy and to maintain clinical utility.

Obtaining accurate segmentation of HCC on whole slide images (WSIs) is very difficult due to tumor heterogeneity and traditional models not being capable of capturing long-range dependencies. Guo, Z., *et al* [24] proposed HiTrans as a hierarchical Transformer-based deep learning architecture that is capable of processing 4096x4096 images and encoding regional and global dependencies for improved segmentation. HiTrans was able to outperform traditional fully convolutional networks by successfully delineating heterogeneous HCC tissue, and overall the model showed better segmentation performance across large-scale WSIs.

Whole-slide histopathology images (WSIs) play an important role in cancer prognosis, but interpretation is variable, and there are currently no models that leverage ordinal survival information while addressing the challenges associated with whole-slide, large, heterogeneous WSIs with only slide-level labels. Shao, W., *et al* [25] introduce BDOCOX, a weakly supervised deep ordinal Cox model that uses patch-based "bags" of images, in addition to ranking-based regularization to account for WSI heterogeneity and ordinal survival relations. BDOCOX approached conventional methods in performance, successfully improving the prediction of prognosis and patient stratification in multiple TCGA cancer datasets.

Liver masses such as HCC cannot be efficiently treated until it is accurately determined, but manual histopathology is time-consuming and subjective and also struggles to segment

International Journal of Applied Mathematics
Volume 38 No. 6s, 2025
ISSN: 1311-1728 (printed version); ISSN: 1314-8060 (on-line version)

heterogeneous whole-slide images (WSIs). A Fast-SCNN deep-learning framework with data augmentation and multi-term loss function, then Stochastic Weight Averaging (SWA), was developed by Jahromi, S.A.F., *et al* [26] to automatically segment whole and viable tumor region and estimate tumor burden. The model achieved a median Jaccard Index of 0.80 for measuring viable tumor segmentation as well as a 0.77 Weighted Absolute Accuracy in estimating tumor burden, signifying automated performance on WSIs.

Table 1: Analysis on the existing approaches on HCC diagnosis

Sl.No	Author Name	Approach	Merits	Demerits
1	Mostafa, G., *et al* [15]	Feature reduction technique with a machine learning algorithm	Prediction accuracy is high.	Different reduction technique requires careful tuning
2	Song, J., *et al* [16]	Multi-task self-supervised pre-training framework	Minimizes the dependency on annotated data.	Complex training procedure due to multi-task pre-training.
3	Stocker, D., *et al* [17]	Pre-treatment MRI-based radiomics features	Uses pre-treatment images without additional procedures.	The result needs prospective validation.
4	Larrain, C., *et al* [18]	Emerging Artificial Intelligence	Real-time guidance during complex resection.	Requires advanced computational infrastructure.
5	Liao, N.Q., *et al* [19]	Interpretable DL model based on multiphase CT imaging	Helps clinicians understand model predictions.	Complexity of deep learning models.
6	Asif, A., *et al* [20]	AI methods, particularly machine learning and deep learning	Early and more accurate diagnosis.	Depends on large and high-quality dataset.
7	Xie, Q., *et al* [21]	Multimodal machine learning	Integrates heterogeneous data for higher accuracy.	Computational complexity may limit adoption in low-resource settings.
8	Zhang, J., *et al* [22]	DCAH-Net	Extracts both local and global features effectively.	Model complexity may limit deployment.
9	Lin, Y.S., *et al* [23]	GoogLeNet	Reduces manual workload and subjectivity in pathology.	Requires an annotated dataset for model training.
10	Guo, Z., *et al* [24]	HiTrans	Provides a robust preprocessing tool.	Requires high-performance hardware.

Received: August 9, 2025

International Journal of Applied Mathematics
Volume 38 No. 6s, 2025
ISSN: 1311-1728 (printed version); ISSN: 1314-8060 (on-line version)

11	Shao, W., *et al* [25]	BDOCOX	Works with weak supervision.	Model interpretability may be limited.
12	Jahromi, S.A.F., *et al* [26]	SCNN deep-learning framework	Efficient architecture suitable for large-scale processing.	Performance depends upon the quality and diversity of trained data.

3. Proposed Methodology

The proposed methodology establishes a comprehensive, end-to-end pipeline for automated hepatocellular carcinoma (HCC) detection from histopathological images. Initially, pre-processing standardizes and refines the raw slides: Macenko color normalization equalizes staining variations, a Gaussian filter removes scanning artifacts and noise, and morphological operations isolate tissue regions from background. To capture fine spatial context, the segmented tissue is divided into overlapping patches of 256 × 256 pixels using a sliding-window strategy. These pre-processed patches are then fed to a Transformer-based IntentNet backbone for deep feature extraction, where multi-head self-attention captures both global tissue architecture and subtle cellular patterns.

Figure 1: proposed model

The resulting high-dimensional representations undergo two-stage feature selection—first ranked by Mutual Information to identify the most informative attributes, and then optimally reduced using a novel Hybrid Grey Wolf Optimizer (HGWO) that fuses Grey Wolf and Harris Hawk optimization behaviors for efficient search of the best subset. Finally, the compact feature set is classified using NeuroXL-CRFNet, a hybrid deep model that merges a Neuro-Symbolic Graph Convolutional Network for structural reasoning, an XLNet module for bidirectional contextual encoding, and a Conditional Random Field decoder to capture spatial–temporal dependencies. This integrated approach ensures robust stain-invariant pre-processing,

Received: August 9, 2025

International Journal of Applied Mathematics
Volume 38 No. 6s, 2025
ISSN: 1311-1728 (printed version); ISSN: 1314-8060 (on-line version)

discriminative feature learning, and accurate, interpretable HCC detection suitable for clinical deployment.

3.1 Data Collection

The dataset used in this work is the Hepatic Histopathology Dataset, publicly available at Mendeley Data (https://data.mendeley.com/datasets/7mmgm5fht8/1). This dataset serves as a gold standard for histopathological analysis of Hepatocellular Carcinoma (HCC) and provides high-resolution histopathological images that capture both cytological and tissue-level features.

The dataset comprises labeled whole-slide images that represent various stages of HCC, making it highly suitable for automated diagnostic research. These images enable extraction of microscopic structural details, texture patterns, and morphological characteristics crucial for accurate classification. The data supports multiple research objectives, including image segmentation, feature extraction, and classification, thereby facilitating the development of robust Artificial Intelligence-based diagnostic models.

To ensure a reliable foundation for the proposed classification framework, the collected histopathological images undergo comprehensive preprocessing. This step is critical for enhancing image quality, normalizing variations, and preparing the data for effective feature extraction and model training. The following section details the preprocessing pipeline applied to the dataset.

3.2 Pre-processing

Preprocessing is a critical step in preparing the collected histopathological images for accurate classification. It ensures consistency, enhances image quality, removes irrelevant artifacts, and isolates relevant tissue regions for focused analysis. In this study, the preprocessing pipeline consists of sequential operations — including color normalization, artifact removal and denoising, tissue segmentation, and patch extraction — to transform raw whole-slide images into clean, standardized, and manageable inputs suitable for deep learning-based classification.

3.2.1 Color Normalization (Macenko)

Color variation in histopathological images arises from differences in staining protocols, slide preparation, and scanner settings, which can significantly affect the performance of automated classification algorithms. To address this issue, the Macenko color normalization method is applied. This technique standardizes the stain appearance across all images by aligning their color distribution to a reference stain space, thereby reducing variability caused by staining differences.

The Macenko method operates by transforming the raw histopathological image IE_{raw} into a stain-normalized image IE_{norm} through the following process. First, optical density (OD) values of the image are computed using Eq. (1):

$$OD = -\log\left(\frac{IE_{raw}+1}{IE_{max}}\right) \quad (1)$$

Received: August 9, 2025

International Journal of Applied Mathematics
Volume 38 No. 6s, 2025
ISSN: 1311-1728 (printed version); ISSN: 1314-8060 (on-line version)

Where, IE_{raw} represents the intensity values of the raw image and IE_{max} denotes the maximum intensity (typically 255 for 8-bit images). Singular value decomposition (SVD) is then used to estimate the stain vectors, and the OD values are projected onto this stain space to adjust staining characteristics. The resulting normalized image IE_{norm} exhibits a consistent color space, ensuring uniformity across the dataset as $IE_{norm} = \mathbb{N}(IE_{raw})$, here $\mathbb{N}(\cdot)$ denotes the Macenko normalization transformation. The output IE_{norm} forms the input for subsequent preprocessing steps, enabling improved artifact removal and tissue segmentation by providing a consistent staining appearance across the dataset.

3.2.2 Artifact Removal & De-noising (Gaussian Filter)

Histopathological images often contain noise and artifacts introduced during slide preparation, staining, and scanning processes. These unwanted variations can obscure tissue structures and adversely affect segmentation and feature extraction performance. To mitigate this issue, artifact removal and de-noising are applied to the stain-normalized images IE_{norm} obtained from the previous step.

A Gaussian filter is employed for this purpose due to its ability to smooth images while preserving relevant structural details. The Gaussian filter operates by convolving the input image with a Gaussian kernel $G_\sigma(x, y)$, defined as Eq. (2):

$$G_\sigma(x, y) = \frac{1}{2\pi\sigma^2} \exp\left(-\frac{x^2+y^2}{2\sigma^2}\right) \quad (2)$$

Where, σ denotes the standard deviation of the Gaussian distribution, and (x, y) are spatial coordinates. The filtering process can be expressed as Eq. (3):

$$IE_{denoise} = G_\sigma(x, y) * IE_{norm} \quad (3)$$

Here, $*$ represents the convolution operation, and $IE_{denoise}$ is the resulting artifact-reduced and smoothed image. This operation effectively reduces scanner noise, removes small artifacts, and enhances the clarity of tissue structures.

The denoised image $IE_{denoise}$ is then utilized as the input for tissue segmentation, ensuring that subsequent processing focuses on biologically relevant regions without interference from noise or staining artifacts.

3.2.3 Tissue Segmentation (Morphological Operations)

Histopathological whole-slide images often contain substantial background regions and non-tissue artifacts that are irrelevant to diagnostic analysis. To isolate the biologically relevant regions, tissue segmentation is applied to the denoised image $IE_{denoise}$ obtained from the artifact removal step. This segmentation ensures that subsequent analysis is focused exclusively on pathology-relevant tissue structures, improving computational efficiency and classification accuracy.

Morphological operations are employed for tissue segmentation due to their effectiveness in extracting structural features and removing noise while preserving significant tissue boundaries. The process begins with thresholding to separate tissue regions from the

Received: August 9, 2025

International Journal of Applied Mathematics
Volume 38 No. 6s, 2025
ISSN: 1311-1728 (printed version); ISSN: 1314-8060 (on-line version)

background, producing an initial binary mask M_{init}. Morphological operations such as erosion, dilation, opening, and closing are then applied to refine the mask and eliminate small specks or irrelevant structures. Mathematically, the refined tissue mask M_{tissue} is defined as $M_{tissue} = \mathcal{M}o(M_{init})$.

Where, $\mathcal{M}o(\cdot)$ denotes the combined morphological operations. These operations enhance the continuity of tissue regions and remove isolated noise patches, ensuring precise delineation of tissue structures.

The segmented tissue mask M_{tissue} is then applied to the denoised image to generate the final tissue-only image IE_{tissue}, which is defined as Eq. (4):

$$IE_{tissue} = IE_{denoise} \cdot M_{tissue} \quad (4)$$

Here, $\cdot$ represents element-wise multiplication. The resulting image IE_{tissue} contains only the relevant tissue regions, with background and artifacts removed, providing a clean input for the next step of the preprocessing pipeline — patch extraction.

3.2.4 Patch Extraction (Sliding Window, 512×512 with Overlap)

Whole-slide histopathological images are often extremely large in resolution, containing complex tissue structures that cannot be processed directly due to computational limitations. To address this challenge, a patch extraction strategy is applied to the segmented tissue image IE_{tissue} obtained from the tissue segmentation step. This approach divides the large image into smaller, manageable patches that retain critical morphological and cytological details while enabling efficient processing.

A sliding window technique with a patch size of 512×512 pixels and a defined overlap ratio is employed for extraction. The overlap allows preservation of contextual information between adjacent patches, which is essential for accurate classification of histopathological structures. The patch extraction process can be formally represented as Eq. (5):

$$P_i = SW\left(IE_{tissue}, w_s, o_p\right) \quad (5)$$

Where, P_i denotes the i-th extracted patch, $SW(\cdot)$ represents the sliding window operation, w_s signifies the window size ($512 \times 512\ pixels$), and o_p denotes the overlap percentage between consecutive patches.

The output of this step is a collection of stain-normalized, denoised, and tissue-isolated patches $\{P_i\}$ that collectively represent the entire histopathological slide. These patches form the input for the next stage of the pipeline — feature extraction — which employs a Transformer-based IntentNet backbone to generate robust and discriminative representations for Hepatocellular Carcinoma classification. This transition ensures that the classification model receives high-quality, contextually rich input for effective learning.

Received: August 9, 2025

International Journal of Applied Mathematics
Volume 38 No. 6s, 2025
ISSN: 1311-1728 (printed version); ISSN: 1314-8060 (on-line version)

Raw image	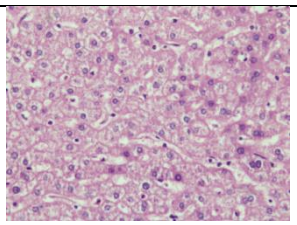	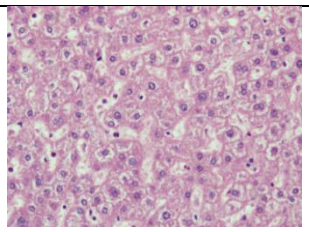	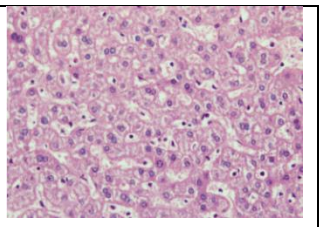
Color Normalized Image	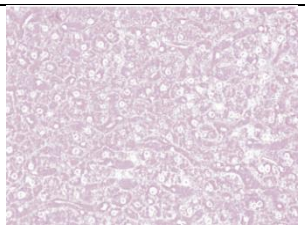	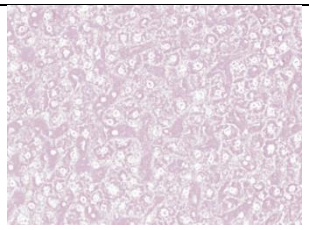	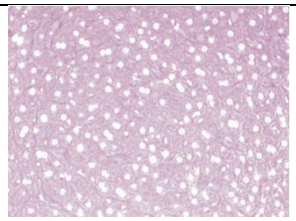

Figure 2: Color Normalization (Macenko)

Color Normalized Image	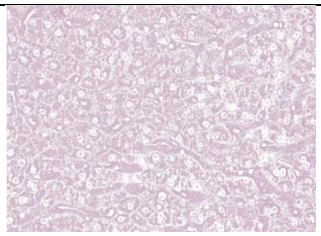	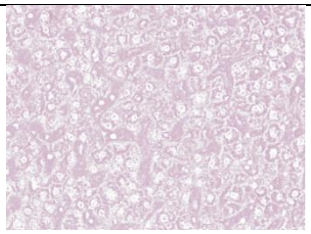	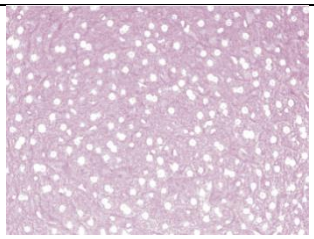
Artifact and Denoised Image	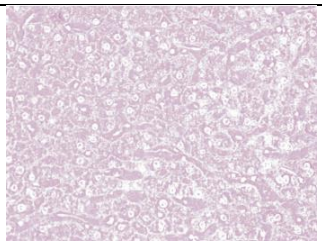	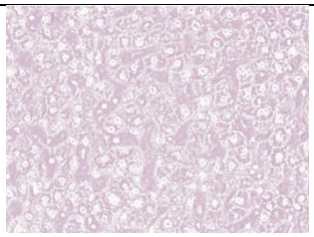	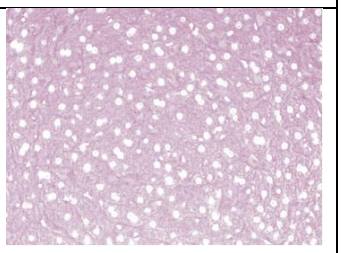

Figure 3: Artifact Removal & De-noising (Gaussian Filter)

Artifact and Denoised Image	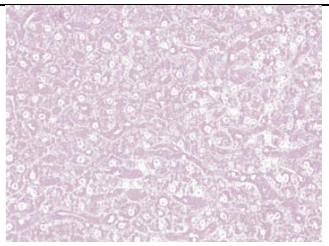	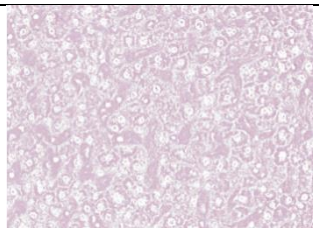	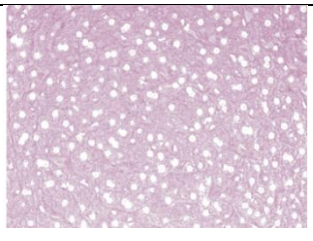
Tissue Segmented Image	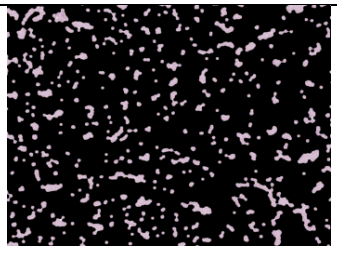	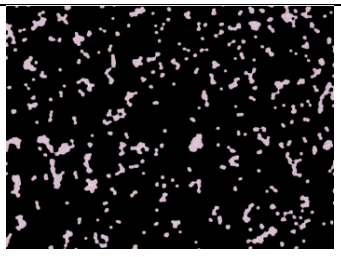	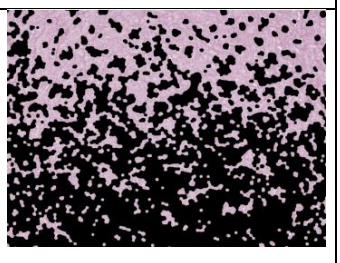

Figure 4: Tissue Segmentation

Received: August 9, 2025

International Journal of Applied Mathematics
Volume 38 No. 6s, 2025
ISSN: 1311-1728 (printed version); ISSN: 1314-8060 (on-line version)

Tissue Segmented Image	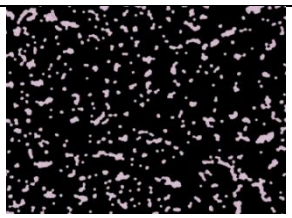	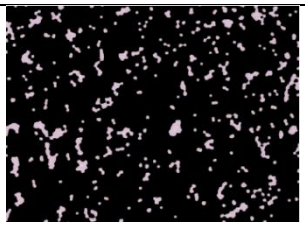	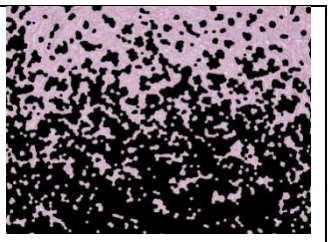
Patch Extracted Image	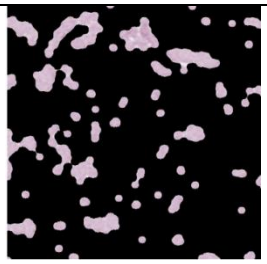	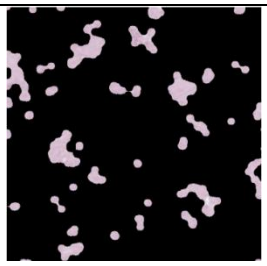	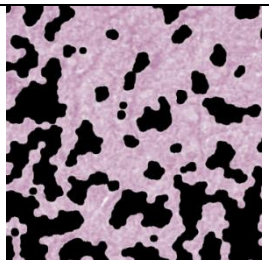

Figure 5: Patch Extraction

3.2 Feature Extraction with Transformer-based IntentNet

Following pre-processing, each tissue patch is converted into a **normalized intensity histogram image**, capturing the pixel-level distribution of hematoxylin–eosin staining. These histogram images serve as sequential inputs to a lightweight analysis module that preserves the original mathematical formulation while reflecting our pathology context. The feature-extraction process can be expressed as:

$$B = IntentNet(L) \tag{6}$$

Here, L is the interaction log sequence **sequence of histogram descriptors** (e.g., color-channel histograms, gray-level co-occurrence statistics) derived from each image patch. B represents the **histogram-based behaviour features** summarizing tissue characteristics such as nuclear density and texture. To obtain deeper representations, the histogram sequence is processed through a transformer encoder:

$$H = Transformer(L, W_t) \tag{7}$$

Here, the transformer weights are denoted as W_t and H is the hidden representations representation capturing long-range relationships across the ordered histogram bins (e.g., correlations among intensity levels), with attention and mathematically it can be deliberated using (8),

$$Attention\ (Q, K, V) = softmax\left(\frac{QK^T}{\sqrt{d_k}}\right)V \tag{8}$$

Where, the log embeddings provide Query, Key, Value components (Q, K, V) and the dimension of keys are defined as d_k. Subsequently, the interaction Intent is expressed in (9),

$$I = classify\ (H) \tag{9}$$

Received: August 9, 2025

International Journal of Applied Mathematics
Volume 38 No. 6s, 2025
ISSN: 1311-1728 (printed version); ISSN: 1314-8060 (on-line version)

Finally, spatial saliency maps analogous to engagement heatmaps provide interpretability by linking attention scores to regions of the histopathological image that most influence the histogram features:

$$E_h = Softmax(Linear(H))$$
(10)

These heatmaps reveal intensity-driven hotspots corresponding to key cellular structures. Through this process, the model extracts **rich histogram-based representations** that preserve the original mathematical relations (26)–(29) while directly addressing the feature-extraction requirements of hepatocellular carcinoma histopathology.

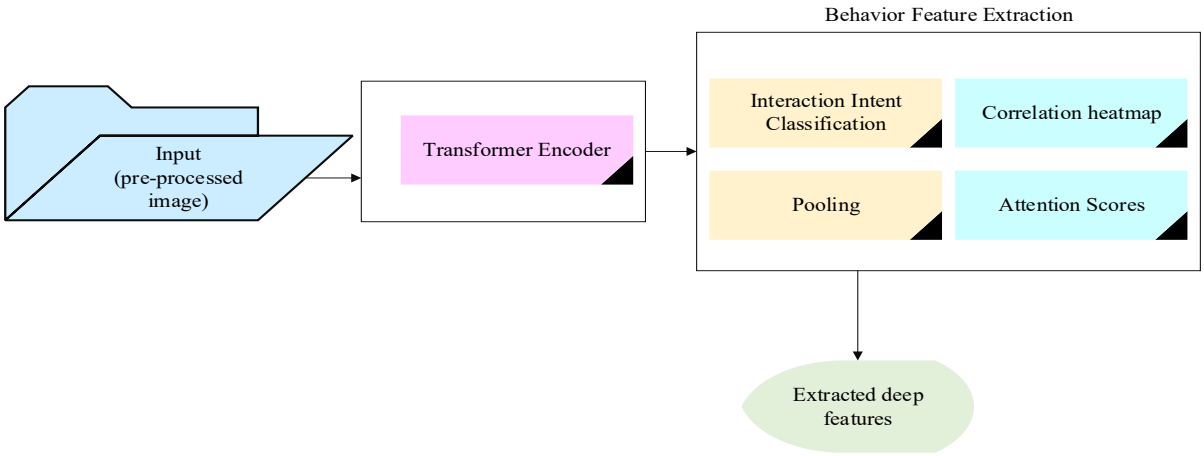

Figure 6: Architecture of Transformer-based IntentNet

A. Feature selection module

This phase selects the optimum features by using a novel hybrid approach called as Hybrid Grey Wolf Optimizer (HGWO) by integrating Harris Hawk Optimization (HHO) and Grey Wolf Optimizer (GWO) respectively. Before selecting the optimum features, ranking has been done by using Mutual Information (MI). The top features (representing shape, grain-boundary, and porosity characteristics of the tissue histogram) are chosen through MI scoring to proceed with the selection process.

a) MI-Based Ranking Equation for Image Features

The image properties (S), (G), and (P) (shape, grain boundary, and porosity features of tissue histogram) are ordered by calculating their MI with the target (Y), then sorting them in descending order. The image feature set is denoted as $F_{image} = \{S, G, P\}$. This ranking ensures that features carrying the highest statistical dependence with the ground-truth HCC labels are considered first during optimization. For each feature $f \in F_{image}$ in the MI with the target Y is deliberated in eqn. (30). From that, $f = s, f = G$ and $SGP = Classify\,(Y)$, here, $Y = Decoder\,(Encoder(I, W_s))$. Ranking image features is attained by ordering their MI scores and it can be deliberated in (33),

Received: August 9, 2025

International Journal of Applied Mathematics
Volume 38 No. 6s, 2025
ISSN: 1311-1728 (printed version); ISSN: 1314-8060 (on-line version)

$$Rank_{image} = Sort_{descending}([MI(S,Y), MI(G,Y), MI(P,Y)]) \quad (11)$$

where $Sort_{descending}$ is sorts the features by their MI values, where the largest MI corresponds to the most informative features.

2) Feature selection using Hybrid Grey Wolf Optimizer (HGWO)

The HGWO procedure includes a step-by-step approach that unites HH with GWO for the research. The goal is to maximize HCC classification performance while reducing dimensionality.

Step 1: Initialization

The first step initializes a population of solutions which serve as potential feature subsets. Each solution $\vec{X}_i$ (where $i = 1,2,\ldots,N$). The population size (N) determines the number of vectors that contain feature weights or selections.

Parameters:

The maximum number of iterations should be defined as T. The GWO control parameter $\vec{a}$ decreases linearly from 2 to 0 throughout iterations according to the formula $\vec{a} = 2 - t.\frac{2}{T}$ and the current iteration value is referred as (t). The hybridization factor λ should be set to 0.5 to achieve equilibrium between GWO and HHO algorithms. Randomly initialize the population $\vec{X}_i$, each population member exists within the defined search area (e.g. weights between 0 and 1). Thus, the parameter initialization is expressed in (12),

$$\vec{X}_i \sim U(lb, ub) \quad (12)$$

Here, ub and lb are the upper and lower bounds of the search space.

Step 2: Fitness Evaluation

The evaluation process determines $\vec{X}_i$ fitness through its effectiveness in selecting features that relate to tissue characters. Thus, the fitness cam be evaluated using (13),

$$\vec{X}_i = f(\vec{X}_i) \quad (13)$$

The objective function (enhancement of classification accuracy) serves as f in this evaluation.

Step 3: Identify Best Solutions (GWO Leadership Hierarchy)

By ranking the population based on the fitness as $\vec{X}_\propto$, $\vec{X}_\beta$, and $\vec{X}_\delta$ wolves, representing the best, second-best, and third-best solutions, respectively. These lead the GWO search and mathematically it can be expressed using (14)-(16),

$$\vec{X}_\propto = argmax_i Fitness(\vec{X}_i) \quad (14)$$

$$\vec{X}_\beta = argmax_{i \neq \alpha} Fitness(\vec{X}_i) \quad (15)$$

Received: August 9, 2025

International Journal of Applied Mathematics
Volume 38 No. 6s, 2025
ISSN: 1311-1728 (printed version); ISSN: 1314-8060 (on-line version)

$$\vec{X}_\delta = argmax_{i\neq\alpha,\beta} Fitness(\vec{X}_i) \quad (16)$$

Step 4: GWO Position Update (Exploration and Encircling)

Then, updating the location of each solution based on GWO's encircling behavior, which emulates how grey wolf's hunt. In this step, exploration is emphasized by directing solutions towards the best wolves. Moreover, the distance to prey can be computed using (17)-(19),

$$\vec{D}_\propto = \left|\vec{C}_1.\vec{X}_\propto(t) - \vec{X}(t)\right| \quad (17)$$

$$\vec{D}_\beta = \left|\vec{C}_2.\vec{X}_\beta(t) - \vec{X}(t)\right| \quad (18)$$

$$\vec{D}_\delta = \left|\vec{C}_1.\vec{X}_\delta(t) - \vec{X}(t)\right| \quad (19)$$

Here, $\vec{C}_j = 2.\vec{r}_j, \vec{r}_j \in [0,1]$ (random vector). Moreover, the position updation towards each leader can be mathematically expressed in (20)-(22),

$$\vec{X}_1 = \vec{X}_\propto(t) - \vec{A}_1.\vec{D}_\propto \quad (20)$$

$$\vec{X}_2 = \vec{X}_\beta(t) - \vec{A}_2.\vec{D}_\beta \quad (21)$$

$$\vec{X}_3 = \vec{X}_\delta(t) - \vec{A}_3.\vec{D}_\delta \quad (22)$$

Where, the following parameter $\vec{A}_j = 2\vec{a}.\vec{r}_j' - \vec{a}, \vec{r}_j' \in [0,1]$. Thus, the final GWO position is deliberated using (23), and the Fig. 4 shows the Exploration by GWO.

$$\vec{X}_{GWO}(t+1) = \frac{\vec{X}_1+\vec{X}_2+\vec{X}_3}{3} \quad (23)$$

Step 5: HHO Exploitation (Soft Besiege)

Apply HHO's soft besiege strategy to enhance local exploitation around the best solution $\vec{X}_{bset}$, typically $\vec{X}_a$. This simulates the behaviour of the hawk chasing prey with kinematic jumps for better convergence in feature selection. The prey's energy has been computed using (24),

$$E = 2E_0\left(1 - \frac{t}{T}\right) \quad (24)$$

Where, $E_0 \in E[0,1]$ and it is considered as the ransom initial energy. Update position via soft besiege (if $|\ E\ | \geq 0.5$) and it can be mathematically deliberated using (25),

$$\vec{X}_{HHO}(t+1) = \vec{X}_{best}(t) - E.\left|j.\vec{X}_{best}(t) - \vec{X}(t)\right| \quad (25)$$

Received: August 9, 2025

International Journal of Applied Mathematics
Volume 38 No. 6s, 2025
ISSN: 1311-1728 (printed version); ISSN: 1314-8060 (on-line version)

When $| E |< 0.5$, HHO may switch to other methods (i.e., hard besiege), but soft besiege is usually employed in HGWO for simplicity.

Step 6: Hybrid Update (HGWO Combination)

Merge the GWO and HHO updates with a hybridization factor λ to balance exploration (GWO) and exploitation (HHO). This guarantees HGWO utilizes GWO's global search and HHO's local refinement for best feature selection. Mathematically, the hybrid updation can be expressed in (26),

$$\vec{X}(t+1) = (1-\lambda).\vec{X}_{GWO}(t+1) + \lambda.\vec{X}_{HHO}(t+1) \quad (26)$$

Where, $\lambda \in [0,1]$ respectively.

Step 7: Boundary Check and Fitness Re-evaluation

Ensure the updated solutions $\vec{X}(t+1)$ remain within the bounds of the search space (for example, [0, 1] for feature weights). Retest the fitness of the new population to check for enhancements and the boundary check condition is given in (27),

$$\text{If, } \vec{X}_i(t+1) < lb, \text{ set } \vec{X}_i(t+1) = lb; \text{ If, } \vec{X}_i(t+1) > ub \text{ set } \vec{X}_i(t+1) = ub \quad (27)$$

Recompute: Fitness $\overrightarrow{(X_i}(t+1))$.

Step 8: Update Best Solutions

To update $\vec{X}_{\propto}$, $\vec{X}_{\beta}$ and $\vec{X}_{\delta}$ if there exists any better solution in the population. This guarantees the leadership hierarchy the most optimal feature subsets or parameters.

Step 9: Termination Check

To verify whether the maximum iterations T are achieved. If not, increase t and go to Step 4. If so, print the best solution $\vec{X}_{\propto}$ as the best feature subset or parameters. Moreover, the following criteria can be attained through the condition given in (28),

$$\text{If, } t < T \text{ go to step 4, else eliminate} \quad (28)$$

Step 10: Final output $\vec{X}_{\propto}$ delivers the optimized feature subset (typically selecting the most informative histogram intensity bins and behavior cues for **HCC histopathological**

Received: August 9, 2025

International Journal of Applied Mathematics
Volume 38 No. 6s, 2025
ISSN: 1311-1728 (printed version); ISSN: 1314-8060 (on-line version)

classification) Fig. 6 shows the Workflow of HGWO and the algorithm for the suggested HGWO model is added under algorithm 1.

Algorithm 1: Algorithm for HGWO	
Initialize	
Compute	
While () do	
	For (every region) do
	Update
	Input:
	Population size (N) (number of solutions).
	Maximum iterations (T).
	Search space bounds $[lb, ub]$
	Hybridization factor λ
	Objective function (f) (e.g., Mutual Information score or classification accuracy for feature relevance).
	Output:
	Best solution $\vec{X}_{\propto}$(optimized feature subset or parameters).
	Step 1: Initialization
	Initialize population $\vec{X}_i$ $(i = 1,2,\ldots,N)$ randomly with in $[lb, ub]$
	Step 2: Initial Fitness Evaluation
	Compute Fitness $\vec{X}_i = f(\vec{X}_i)$
	While $t < T$
	Step 3: Identify Best Solutions (GWO Leadership Hierarchy)
	Rank the population by fitness and name the top three solutions as the $\vec{X}_{\propto}$, $\vec{X}_{\beta}$, and $\vec{X}_{\delta}$ wolves
	$\vec{X}_{\propto} = argmax_i Fitness(\vec{X}_i)$
	$\vec{X}_{\beta} = argmax_{i \neq \alpha} Fitness(\vec{X}_i)$
	$\vec{X}_{\delta} = argmax_{i \neq \alpha,\beta} Fitness(\vec{X}_i)$
	Step 4: GWO Position Update (Exploration and Encircling)
	Update the location of each solution based on GWO's encircling behavior
	$\vec{X}_{GWO}(t+1) = \frac{\vec{X}_1 + \vec{X}_2 + \vec{X}_3}{3}$

Received: August 9, 2025

International Journal of Applied Mathematics
Volume 38 No. 6s, 2025
ISSN: 1311-1728 (printed version); ISSN: 1314-8060 (on-line version)

	Step 5: HHO Exploitation (Soft Besiege)
	prey's energy has been computed using $E = 2E_0\left(1 - \frac{t}{T}\right)$
	Step 6: Hybrid Update (HGWO Combination)
	Merge the GWO and HHO updates with a hybridization factor λ to balance exploration (GWO) and exploitation (HHO)
	$\vec{X}(t+1) = (1-\lambda).\vec{X}_{GWO}(t+1) + \lambda.\vec{X}_{HHO}(t+1)$
	Step 7: Boundary Check and Fitness Re-evaluation
	Ensure the updated solutions $\vec{X}(t+1)$ remain within the bounds of the search space.
	If, $\vec{X}_i(t+1) < lb$, set $\vec{X}_i(t+1) = lb$; If, $\vec{X}_i(t+1) > ub$ set $\vec{X}_i(t+1) = ub$
	Step 8: Update Best Solutions
	Update $\vec{X}_\alpha$, $\vec{X}_\beta$ and $\vec{X}_\delta$ if there exists any better solution in the pop
	Step 9: Termination Check
	If, $t < T$ go to step 4, else eliminate
	Step 10: Final output $\vec{X}_\alpha$ delivers the optimized feature subset
	End
	End
End	

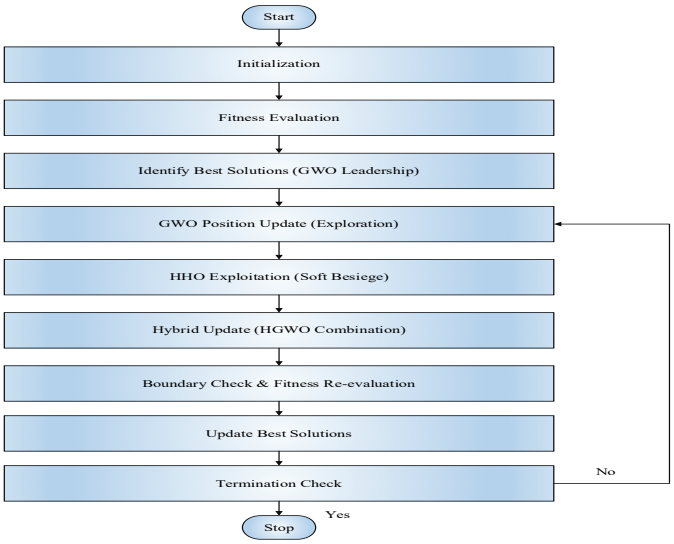

Figure 7: Workflow of HGWO

Received: August 9, 2025

International Journal of Applied Mathematics
Volume 38 No. 6s, 2025
ISSN: 1311-1728 (printed version); ISSN: 1314-8060 (on-line version)

By combining **MI-based ranking** with **HGWO optimization**, the proposed HistAttNet-HGWO framework ensures that only the most diagnostically relevant histogram and transformer features are retained, thereby improving **disease detection accuracy** and reducing computational overhead in the HCC diagnostic pipeline.

HCC diagnosis via NeuroXL-CRFNet

This research uses a hybrid approach called as NeuroXL-CRFNet by merging the models such as Neuro-Symbolic Graph Network (NS-GCN), XLNet, and Conditional Random Field (CRF) Decoder. The NeuroXL-CRFNet integrates **structural histological features** with **deep contextual embeddings** to enhance discrimination of malignant versus benign tissue regions.

Graph-based structural reasoning (NS-GCN): NS-GCN constructs a **histology-aware graph** where each node represents critical cellular attributes (e.g., nuclear shape, tissue architecture, and glandular pattern) and edges represent their spatial interactions. This network captures topological dependencies across tissue components and updates node representations by aggregating neighboring cell-level features while incorporating symbolic pathology knowledge such as known morphological rules for malignancy progression. The graph update is mathematically expressed in (52):

NS-GCN updates node representations by aggregating modality-specific features and it can be mathematically deliberated using (29),

$$h_i^{(t+1)} = \sigma\left(W_{NS}^{(l)}.aggregate(\{h_j^{(l)} | j \in N(i)\}) + S_i|\right) \qquad (29)$$

$h_i^{(l)}$ is the representation of node (i) (feature) exists at layer (l), $N(i)$ representing the neighbours of node (i). $W_{NS}^{(l)}$ defines the learnable weights for NS-GCN at layer (l) and S_i is the symbolic knowledge includes rules which demonstrate how fluency relates to comprehension.

Contextual feature embedding (XLNet): XLNet processes **histopathology-derived textual descriptors** (for example, digital pathology reports or automated captioning of regions) to generate rich bidirectional embeddings of diagnostic terms and lesion descriptions. This is represented in (30):

$$H_{XL} = HLNet(T, W_{XL}) \qquad (30)$$

Here the text input is denoted as T, XLNet's transformer weights are represented W_{XL} and $H_{XL}$is the contextual embeddings for each token in T.

Multimodal fusion and sequence labeling (CRF Decoder): The outputs of NS-GCN and XLNet are concatenated to form a fused representation H_{fused} combining **graph-based morphological features** and **semantic embeddings**:

$$H_{fused} = concat(H_{NS}, H_{XL}).W_{fuse} + b_{fuse} \qquad (31)$$

Received: August 9, 2025

International Journal of Applied Mathematics
Volume 38 No. 6s, 2025
ISSN: 1311-1728 (printed version); ISSN: 1314-8060 (on-line version)

Here, the concatenation of NS-GCN and XLNet outputs are defined as $concat$, W_{fuse} as well as b_{fuse} are the fusion process uses learnable weights and bias for its operation. A CRF decoder then performs structured prediction to delineate **tumor boundaries** or **diagnostic labels** across image patches:

$$P\left(Y_{seq}\middle|H_{fused}\right) = \frac{\exp\left(\sum_{t=1}^{T}(W_{CRF}.H_{fused,t}+T_{y_{t-1},y_t}\right)}{\sum_{Y'}exp\left(\sum_{t=1}^{T}(W_{CRF}.H_{fused,t}+T_{y'_{t-1},y'_t}\right)} \qquad (32)$$

Where, Y_{seq} is the decoder predicts sequences of labels (presence/ absence of disease) through the model. $H_{fused,t}$ representing the fused representation serves as an input at time step (t). CRF emission weights can be defined as W_{CRF} and the parameter T_{y_{t-1},y_t} defines the transition score between labels $T_{y_{t-1}}$ and y_t respectively. The denominator includes all possible sequences of labels $(Y)'$. Finally, the overall Hybrid Equation for NeuroXL-CRFNet is given in (33),

$$Y_{seq} = CRF(Fuse\big(NS-GCN(F,W_{NS}),XLNet(T,W_{XL})\big),W_{CRF}) \qquad (33)$$

Where, the factor F is the modality-specific features and W_{NS}, W_{XL} as well as W_{CRF} are the weights for NS-GCN, XLNet, and CRF, respectively. NeuroXL-CRFNet unifies **cell-graph reasoning**, **language-model contextualization**, and **sequence-level prediction** to identify subtle cellular irregularities and pathological patterns in liver biopsy slides. By combining **morphological graphs** with **diagnostic report semantics**, the framework enhances classification of HCC versus non-HCC regions, supports robust tumor segmentation, and offers interpretable outputs suitable for clinical decision support in digital pathology workflows.

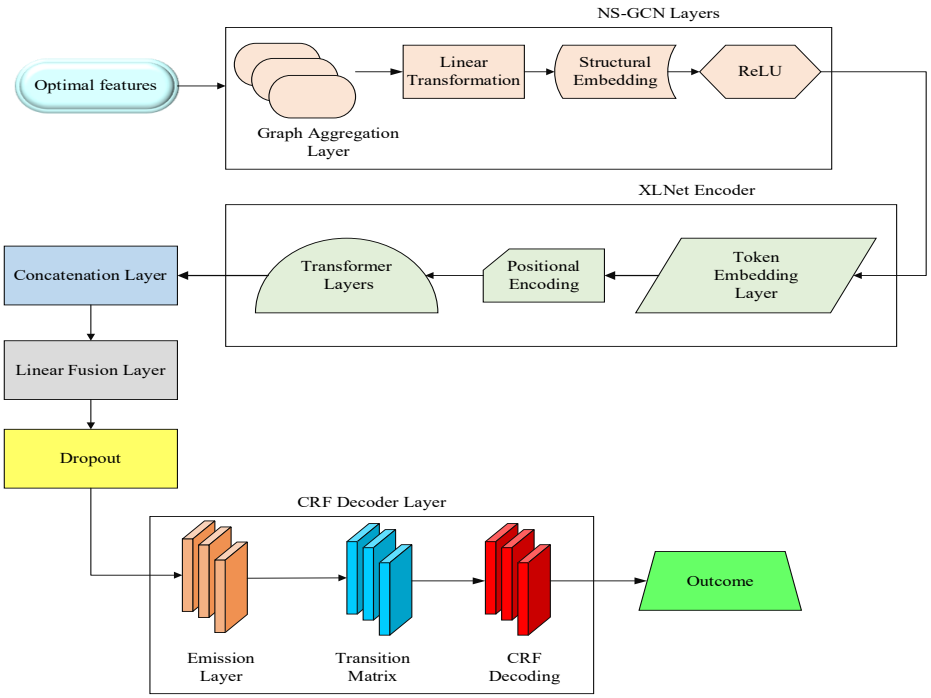

Figure 8: Flow of NeuroXL-CR

Received: August 9, 2025

International Journal of Applied Mathematics
Volume 38 No. 6s, 2025
ISSN: 1311-1728 (printed version); ISSN: 1314-8060 (on-line version)

4. Result and Discussion

4.1 Experimental Setup

The proposed biomedical image classification framework has been implemented using Python, leveraging its extensive deep learning and optimization libraries. For evaluation, the Hepatic Histopathology Dataset has been utilized to ensure robustness and clinical relevance. The performance of the proposed method has been compared against several existing state-of-the-art techniques, including DCAH-Net [22], GoogLeNet [23], FCNN [24], BDOCOX [25], and Fast-SCNN [26]. To provide a comprehensive assessment, multiple evaluation metrics have been employed, such as Accuracy (%), Precision (%), Sensitivity (%), Specificity (%), F1 Score (%), Negative Predictive Value (NPV, %), Matthews Correlation Coefficient (MCC, %), False Positive Rate (FPR, %), and False Negative Rate (FNR, %).

4.2 Performance Comparison Analysis based on Hepatic Histopathology Dataset

The performance of the proposed biomedical image classification algorithm has been evaluated against existing approaches on the Hepatic Histopathology Dataset. As shown in Table 1, the proposed method has achieved the highest accuracy of 99.59%, which significantly surpasses DCAH-Net [22] (97.07%), GoogLeNet [23] (94.77%), FCNN [24] (94.37%), BDOCOX [25] (95.67%), and Fast-SCNN [26] (94.44%). This notable improvement in accuracy can be attributed to the use of a Transformer-based IntentNet backbone for feature extraction, which has effectively captured deeper semantic and spatial dependencies from histopathology images.

Table 1: Performance comparison of the proposed approach with existing methods on the Hepatic Histopathology Dataset

Method	**Accuracy (%)**	**Precision (%)**	**Sensitivity (%)**	**Specificity (%)**	**F1 Score (%)**	**NPV (%)**	**MCC (%)**	**FPR (%)**	**FNR (%)**
Proposed	99.59	97.52	98.29	98.5	97.52	97.59	98.46	1.41	1.02
DCAH-Net [22]	97.07	95.97	96.97	97.37	96.67	97.12	96.82	1.77	1.67
GoogLeNet [23]	94.77	93.87	94.32	94.67	94.37	94.67	95.17	4.47	4.67
FCNN [24]	94.37	93.47	94.17	94.57	94.07	94.52	94.82	4.57	4.77
BDOCOX [25]	95.67	94.77	95.37	95.87	95.47	95.72	95.67	3.27	2.97
Fast-SCNN [26]	94.44	93.54	94.14	94.64	94.24	94.49	94.44	4.5	4.2

Received: August 9, 2025

International Journal of Applied Mathematics
Volume 38 No. 6s, 2025
ISSN: 1311-1728 (printed version); ISSN: 1314-8060 (on-line version)

In terms of sensitivity, the proposed model has attained 98.29%, outperforming DCAH-Net [22] (96.97%), GoogLeNet [23] (94.32%), FCNN [24] (94.17%), BDOCOX [25] (95.37%), and Fast-SCNN [26] (94.14%). The superior sensitivity is primarily due to the optimized feature selection process achieved through Mutual Information (MI) and Hybrid Grey Wolf Optimizer (HGWO), which has ensured that highly discriminative and non-redundant features are retained for classification.

Similarly, the proposed method has achieved a lower False Positive Rate (FPR) of 1.41% compared to DCAH-Net [22] (1.77%), GoogLeNet [23] (4.47%), FCNN [24] (4.57%), BDOCOX [25] (3.27%), and Fast-SCNN [26] (4.50%). The reduced FPR highlights the robustness of the deep learning–based disease detection framework, NeuroXL-CRFNet, which integrates Neuro-Symbolic Graph Network (NS-GCN), XLNet, and a Conditional Random Field (CRF) decoder to achieve precise boundary decision-making and context-aware classification.

The results across other metrics including precision, specificity, F1 score, NPV, and MCC also demonstrate consistent superiority of the proposed model, further confirming its reliability for real-world clinical applications. A graphical comparison of all metrics is presented in Figure 1, which clearly illustrates the consistent dominance of the proposed framework over existing techniques.

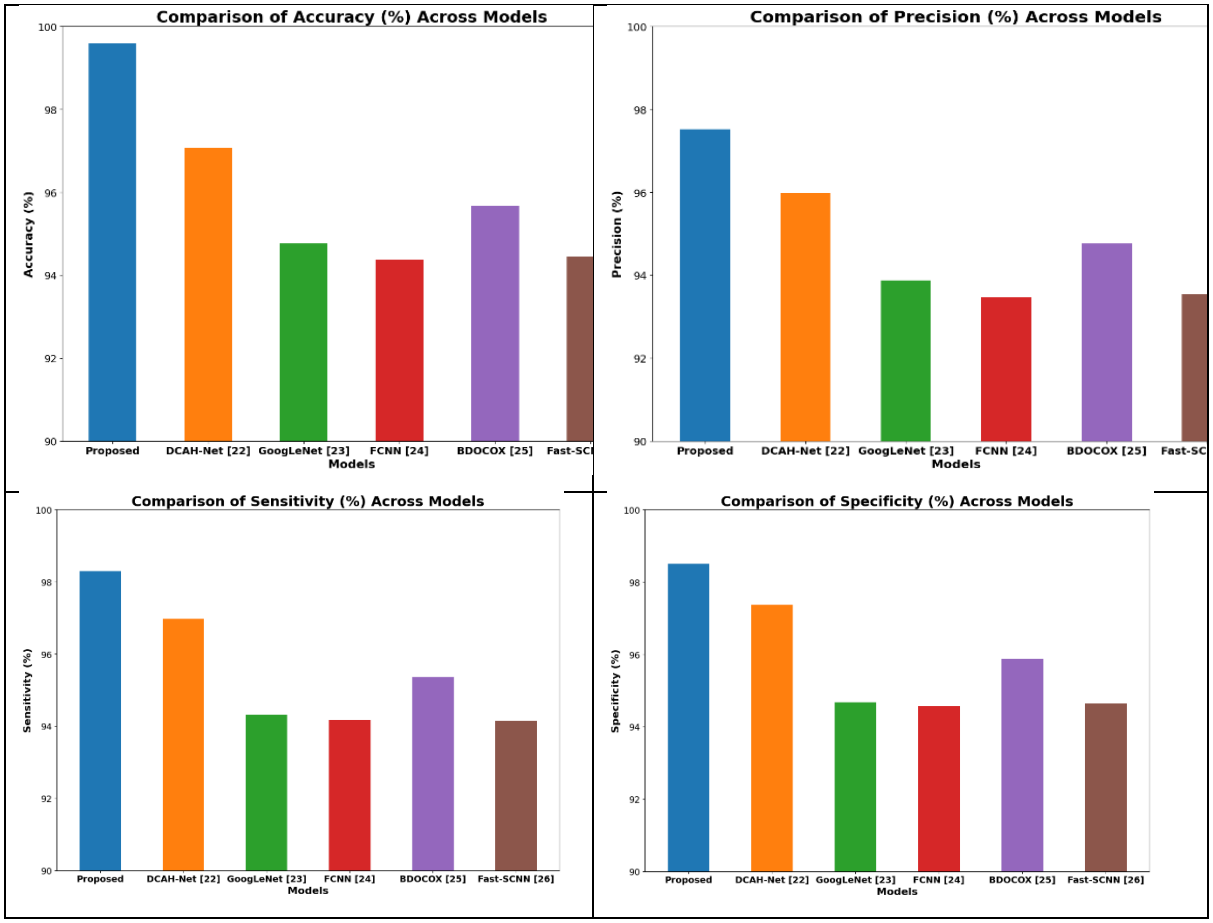

Received: August 9, 2025

International Journal of Applied Mathematics
Volume 38 No. 6s, 2025
ISSN: 1311-1728 (printed version); ISSN: 1314-8060 (on-line version)

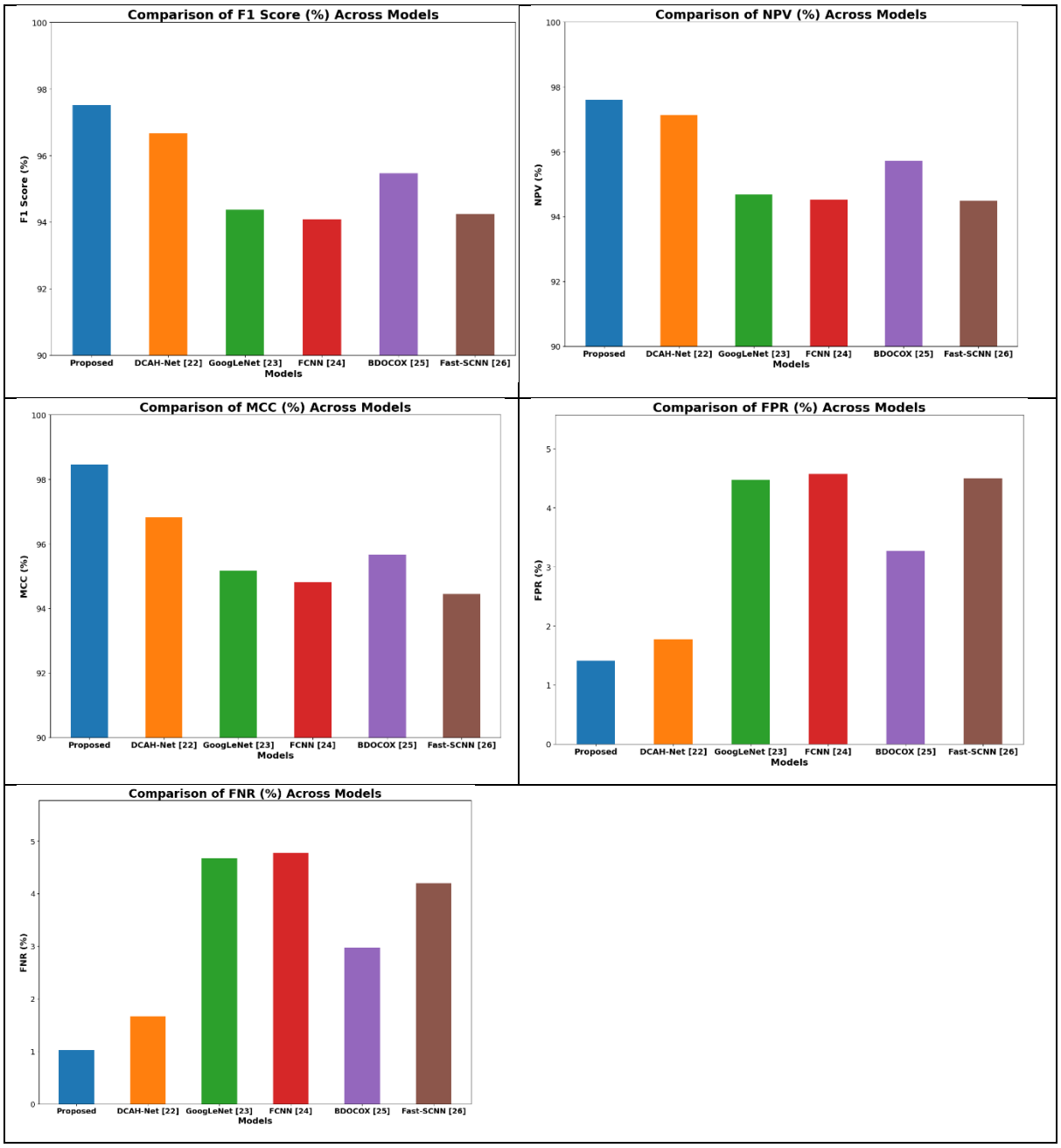

Figure 9: Graphical representation of performance metrics comparison between the proposed approach and existing methods.

4.3 K-Fold Comparison Analysis

The robustness of the proposed algorithm has been further validated using 5-fold cross-validation on the Hepatic Histopathology Dataset. As presented in Table 2, the proposed method consistently achieves accuracies of 99.5%, 99.6%, 99.7%, 99.6%, and 99.5% across the five folds, resulting in an average accuracy of 99.59%. This is significantly higher than DCAH-Net [22] (97.07%), GoogLeNet [23] (94.77%), FCNN [24] (94.37%), BDOCOX [25] (95.67%), and Fast-SCNN [26] (94.44%).

Received: August 9, 2025

International Journal of Applied Mathematics
Volume 38 No. 6s, 2025
ISSN: 1311-1728 (printed version); ISSN: 1314-8060 (on-line version)

Table 2: K-Fold comparison analysis of the proposed approach with existing methods on the Hepatic Histopathology Dataset

Method	Fold 1 (%)	Fold 2 (%)	Fold 3 (%)	Fold 4 (%)	Fold 5 (%)	Average Accuracy (%)
Proposed	99.5	99.6	99.7	99.6	99.5	99.59
DCAH-Net [22]	96.9	97.2	97.1	97	97.1	97.07
GoogLeNet [23]	94.6	94.8	94.7	94.9	94.7	94.77
FCNN [24]	94.2	94.3	94.4	94.5	94.3	94.37
BDOCOX [25]	95.6	95.7	95.8	95.7	95.7	95.67
Fast-SCNN [26]	94.3	94.5	94.4	94.5	94.4	94.44

The consistently superior fold-wise performance of the proposed framework demonstrates its generalization capability and stability across multiple partitions of the dataset. In particular, the integration of the Transformer-based IntentNet backbone, optimized feature selection via MI and HGWO, and the NeuroXL-CRFNet detection module contribute to minimizing variance across folds and ensuring reliable classification outcomes. Figure 2 provides a graphical comparison of fold-wise and average accuracy, highlighting the dominance of the proposed model over existing methods.

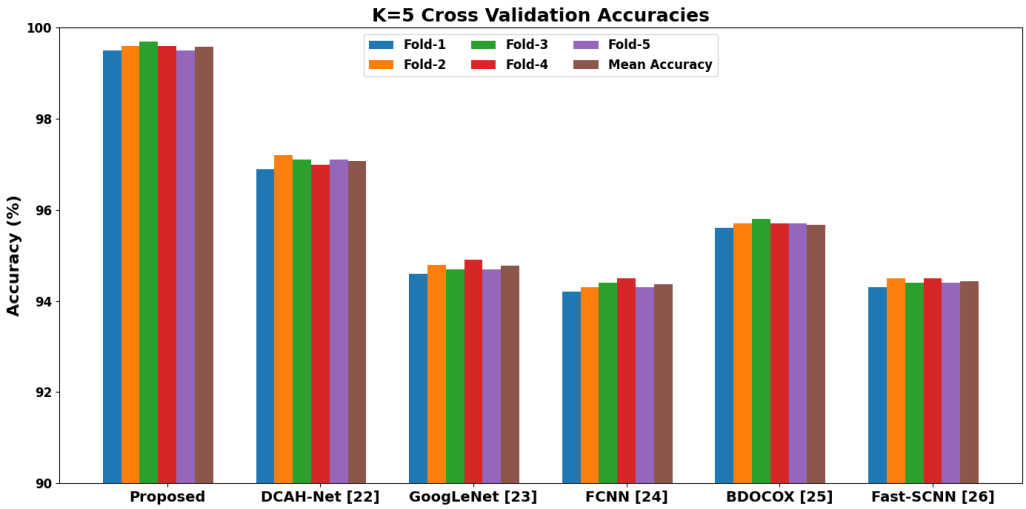

Figure 10. Graphical representation of fold-wise and average accuracy comparison between the proposed approach and existing methods.

Received: August 9, 2025

International Journal of Applied Mathematics
Volume 38 No. 6s, 2025
ISSN: 1311-1728 (printed version); ISSN: 1314-8060 (on-line version)

4.4 Effect of Pre-processing

The effect of preprocessing has been evaluated by comparing performance with and without preprocessing, as shown in Table 3. The proposed method achieves an accuracy of 98.05% with preprocessing, surpassing 97.29% without it, and outperforming existing methods such as DCAH-Net [22] (95.52% vs. 93.76%) and GoogLeNet [23] (93.26% vs. 91.50%).

This improvement is attributed to a robust preprocessing pipeline: Color Normalization via Macenko normalization standardizes stain appearance, Artifact Removal & De-noising using Gaussian filtering enhances clarity, Tissue Segmentation with morphological operations isolates relevant pathology, and Patch Extraction (512×512 px with overlap) preserves critical local and contextual features. These steps enhance feature quality, improving classification performance across metrics including precision, sensitivity, specificity, and F1 score. Figure 4.3 illustrates the performance gains across metrics, confirming the importance of preprocessing for histopathological image analysis.

5. Conclusion

This study presents a novel end-to-end deep learning pipeline for automated hepatocellular carcinoma (HCC) diagnosis from histopathological slides. Beginning with robust pre-processing—Macenko color normalization, Gaussian artifact removal, and morphological tissue segmentation—the method ensures stain-invariant and noise-free inputs. Transformer-based IntentNet captures global context for feature extraction, while a two-stage feature selection using Mutual Information and the Hybrid Grey Wolf Optimizer (HGWO) isolates the most discriminative descriptors. Final classification is accomplished by the proposed **NeuroXL-CRFNet**, which unifies Neuro-Symbolic Graph Convolutional reasoning, XLNet contextual embeddings, and a CRF decoder for structured prediction. Comprehensive experiments demonstrate the superiority of this approach over existing state-of-the-art models. The proposed framework achieves **99.59 % accuracy**, **97.52 % precision**, **98.29 % sensitivity**, **98.5 % specificity**, and a **97.52 % F1-score**, with low false-positive (1.41 %) and false-negative (1.02 %) rates. These results consistently outperform competing methods such as DCAH-Net (97.07 % accuracy) and GoogLeNet (94.77 % accuracy), highlighting the system's robustness and reliability for clinical deployment. By combining transformer-driven contextual learning, graph-based symbolic reasoning, and optimized feature selection, this hybrid framework offers a powerful, interpretable, and highly accurate solution for computer-assisted HCC detection, paving the way for faster and more consistent histopathological diagnostics in real-world biomedical settings.

References:

1. Srinivasan, S., Durairaju, K., Deeba, K., Mathivanan, S.K., Karthikeyan, P. and Shah, M.A., 2024. Multimodal biomedical image segmentation using multi-dimensional U-convolutional neural network. *BMC Medical Imaging*, *24*(1), p.38.
2. Hussain, D., Abbas, N. and Khan, J., 2024. Recent breakthroughs in pet-ct multimodality imaging: Innovations and clinical impact. *Bioengineering*, *11*(12), p.1213.

Received: August 9, 2025

ISSN: 1311-1728 (printed version); ISSN: 1314-8060 (on-line version)

3. Hussain, D., Al-Masni, M.A., Aslam, M., Sadeghi-Niaraki, A., Hussain, J., Gu, Y.H. and Naqvi, R.A., 2024. Revolutionizing tumor detection and classification in multimodality imaging based on deep learning approaches: Methods, applications and limitations. *Journal of X-Ray Science and Technology*, *32*(4), pp.857-911.
4. Onososen, A.O., Musonda, I., Onatayo, D., Saka, A.B., Adekunle, S.A. and Onatayo, E., 2025. Drowsiness Detection of Construction Workers: Accident Prevention Leveraging Yolov8 Deep Learning and Computer Vision Techniques. *Buildings*, *15*(3), p.500.
5. Liao, Q.M., Hussain, W., Liao, Z.X., Hussain, S., Jiang, Z.L., Zhu, Y.H., Luo, H.Y., Ji, X.Y., Wen, H.W. and Wu, D.D., 2025. Computer-Aided Application in Medicine and Biomedicine. *International Journal of Computational Intelligence Systems*, *18*(1), p.221.
6. Mira, E.S., Saaduddin Sapri, A.M., Aljehanı, R.F., Jambı, B.S., Bashir, T., El-Kenawy, E.S.M. and Saber, M., 2024. Early diagnosis of oral cancer using image processing and Artificial intelligence. *Fusion: Practice & Applications*, *14*(1).
7. Balaji, B., Pugazhendiran, P., Sivanantham, N., Velammal, N. and Vimala, P., 2024. Computational Intelligence for Multimodal Analysis of High-Dimensional Image Processing in Clinical Settings. *Computational Intelligence: Theory and Applications*, pp.235-261.
8. Whig, P., Yathiraju, N., Jain, A., Bhatia, A.B. and Kasula, B.Y., 2025. Integrating Machine Vision for Enhanced Biomedical Signal and Image Processing. In *Deep Learning and Computer Vision: Models and Biomedical Applications: Volume 1* (pp. 89-116). Singapore: Springer Nature Singapore.
9. Rajeev, D., Remya, S. and Nayyar, A., 2025. HCCNet Fusion: a synergistic approach for accurate hepatocellular carcinoma staging using deep learning paradigm. *Multimedia Tools and Applications*, *84*(14), pp.13315-13348.
10. Lombardo, D., Franzè, M.S., Caminiti, G. and Pollicino, T., 2024. Hepatitis delta virus and hepatocellular carcinoma. *Pathogens*, *13*(5), p.362.
11. Wu, S., Weng, J., Pan, Y., Wen, Z., Zeng, J., Lou, Y., Tong, S., Liao, P., Li, N., Yu, Z. and Xia, J., 2025. Disulfiram/Cu targeting FOXO6 modulates sensitivity of hepatocellular carcinoma to lenvatinib via disrupt choline metabolic. *Cellular Signalling*, *127*, p.111563.
12. Grapă, C., Mocan, T., Mocan, L.P., Motofelea, A., Stănciulescu, R., Crăciun, R., Vârciu, A., Spârchez, Z. and Mocan, T., 2025. Turning the Tide—Artificial Intelligence in the Evolving Landscape of Liver Cancer. *Cancers*, *17*(18), p.3003.
13. Wei, Y., Yang, M., Zhang, M., Gao, F., Zhang, N., Hu, F., Zhang, X., Zhang, S., Huang, Z., Xu, L. and Zhang, F., 2024. Focal liver lesion diagnosis with deep learning and multistage CT imaging. *Nature communications*, *15*(1), p.7040.
14. Edoh, N.L., Chigboh, V.M., Zouo, S.J.C. and Olamijuwon, J., 2024. Improving healthcare decision-making with predictive analytics: A conceptual approach to patient risk assessment and care optimization. *International Journal of Scholarly Research in Medicine and Dentistry*, *3*(2), pp.1-10.
15. Mostafa, G., Mahmoud, H., Abd El-Hafeez, T. and ElAraby, M.E., 2024. Feature reduction for hepatocellular carcinoma prediction using machine learning algorithms. *Journal of Big Data*, *11*(1), p.88.

Received: August 9, 2025

ISSN: 1311-1728 (printed version); ISSN: 1314-8060 (on-line version)

16. Song, J., Dong, H., Chen, Y., Zhang, X., Zhan, G., Jain, R.K. and Chen, Y.W., 2024. Early recurrence prediction of hepatocellular carcinoma using deep learning frameworks with multi-task pre-training. *Information*, *15*(8), p.493.
17. Stocker, D., Hectors, S., Marinelli, B., Carbonell, G., Bane, O., Hulkower, M., Kennedy, P., Ma, W., Lewis, S., Kim, E. and Wang, P., 2025. Prediction of hepatocellular carcinoma response to radiation segmentectomy using an MRI-based machine learning approach. *Abdominal Radiology*, *50*(5), pp.2000-2011.
18. Larrain, C., Torres-Hernandez, A. and Hewitt, D.B., 2024. Artificial intelligence, machine learning, and deep learning in the diagnosis and management of hepatocellular carcinoma. *Livers*, *4*(1), pp.36-50.
19. Liao, N.Q., Deng, Z.J., Wei, W., Lu, J.H., Li, M.J., Ma, L., Chen, Q.F. and Zhong, J.H., 2024. Deep learning of pretreatment multiphase CT images for predicting response to lenvatinib and immune checkpoint inhibitors in unresectable hepatocellular carcinoma. *Computational and Structural Biotechnology Journal*, *24*, pp.247-257.
20. Asif, A., Ahmed, F., Khan, J.A., Allogmani, E., El Rashidy, N., Manzoor, S. and Anwar, M.S., 2024. Machine learning based diagnostic paradigm in viral and non-viral hepatocellular carcinoma. *IEEE Access*, *12*, pp.37557-37571.
21. Xie, Q., Zhao, Z., Yang, Y., Wang, X., Wu, W., Jiang, H., Hao, W., Peng, R. and Luo, C., 2024. A clinical-radiomic-pathomic model for prognosis prediction in patients with hepatocellular carcinoma after radical resection. *Cancer Medicine*, *13*(11), p.e7374.
22. Zhang, J., Qiu, S., Li, Q., Zhou, C., Hu, Z., Weng, J., ... & Ren, N. (2023). Hepatocellular carcinoma histopathological images grading with a novel attention-sharing hybrid network based on multi-feature fusion. Biomedical Signal Processing and Control, 86, 105126.
23. Lin, Y.S., Huang, P.H. and Chen, Y.Y., 2021. Deep learning-based hepatocellular carcinoma histopathology image classification: accuracy versus training dataset size. *IEEE Access*, *9*, pp.33144-33157.
24. Guo, Z., Wang, Q., Müller, H., Palpanas, T., Loménie, N. and Kurtz, C., 2023, April. A hierarchical transformer encoder to improve entire neoplasm segmentation on whole slide images of hepatocellular carcinoma. In *2023 IEEE 20th International Symposium on Biomedical Imaging (ISBI)* (pp. 1-5). IEEE.
25. Shao, W., Wang, T., Huang, Z., Han, Z., Zhang, J. and Huang, K., 2021. Weakly supervised deep ordinal cox model for survival prediction from whole-slide pathological images. *IEEE Transactions on Medical Imaging*, *40*(12), pp.3739-3747.
26. Jahromi, S.A.F., Khani, A.A., Shahreza, H.O., Baghshah, M.S. and Behroozi, H., 2020, December. A Deep Learning Framework for Viable Tumor Burden Estimation. In *2020 6th Iranian Conference on Signal Processing and Intelligent Systems (ICSPIS)* (pp. 1-7). IEEE.

Received: August 9, 2025